Improved Transient Modeling and Stability Analysis for Grid-Following Wind Turbine: Third-Order Sequence Mapping EAC

Li, Ruibo; Yan, Xiangwu; Wang, Yanbo; Zhang, Qi; Chen, Zhe

Published in:
IEEE Transactions on Power Delivery

DOI (link to publication from Publisher):
10.1109/TPWRD.2024.3355901

Publication date:
2024

Document Version
Accepted author manuscript, peer reviewed version

Improved Transient Modeling and Stability Analysis for Grid-Following Wind Turbine: Third-Order Sequence Mapping EAC

Ruibo Li, *Student Member, IEEE*, Xiangwu Yan, *Member, IEEE*, Yanbo Wang, *Senior Member, IEEE*, Qi Zhang, *Student Member, IEEE*, and Zhe Chen, *Fellow, IEEE*

***Abstract*—The increasing penetration of wind power leads to diverse stability issues, which present more extreme fluctuation and nonlinearity, especially under a weak grid. For the nonlinear transient process, it is particularly complex to estimate since no analytical solution can be found in math. To determine the transient stability of the grid-following (GFL) wind turbine, this article develops a third-order transient model of the GFL-doubly fed induction generator, which consists of a second-order phase-locked loop model and a first-order active power control model. Then, a motion discretization equal area criterion (MD-EAC) method is proposed to estimate the damping effect in the second-order system, which could enhance transient trajectory accuracy and improve stable region reliability. Based on MD-EAC, a power angle to time sequence mapping EAC (SM-EAC) method is proposed to perform the stability analysis in third-order systems with active power control. Finally, numerical simulation results are given to validate the effectiveness of the proposed MD-EAC and SM-EAC under various scenarios. And the mechanism of multi-swing stability is analyzed by numerical simulation and SM-EAC.**

***Index Terms*—Damping, Equal area criterion, Phase-locked loop, Sequence mapping, Third-order, Transient stability.**

NOMENCLATURE

I_s, I_r	Stator and rotor current.
U_s, E_s	Stator terminal and generated voltage.
U_g	PCC voltage.
L_m, X_m	Mutual inductance and reactance.
L_s, X_s	Stator inductance and reactance.
X_l	Line reactance.
ω_s, ω_n	Electrical angular velocity of stator and rated electrical angular velocity of PCC voltage.
θ_{mec}	Rotor mechanical angular position.
θ_{pll}, θ_g	PLL output angular position and PCC voltage angular position.
δ, ω	Power angle and its angular velocity.
δ_{step}	Step size of power angle.
k_{pp}, k_{pi}	Proportional and integral parameters of PLL.
k_{ap}, k_{ai}	Proportional and integral parameters of active power control.
I_{max}	Maximum rotor current.
I_{ms}	Stator excitation current
P_s	Stator output active power.
P	Park transform matrix.
E_k, E_p, E_d	Equivalent kinetic, potential, and damping energy.
P_{em}, P_{em}, P_{ed}	Equivalent mechanical, electromagnetic and damping power
Subscripts	
d, q	Direct and quadrature axis components.
ref	Reference value.

This work was supported by Beijing Natural Science Foundation under Grant 3212037 and State Key Laboratory of Alternate Electrical Power System with Renewable Energy Sources under Grant NO.LAPS21021. *(Corresponding author: Xiangwu Yan.)*

Ruibo Li is both with the Key Laboratory of Distributed Energy Storage and Microgrid of Hebei Province, North China Electric Power University, Baoding 071003, China and the Department of Energy Technology, Aalborg University, Aalborg 9220, Denmark. (e-mail: rb_li@ncepu.edu.cn;)

Xiangwu Yan is with the Key Laboratory of Distributed Energy Storage and Microgrid of Hebei Province, North China Electric Power University, Baoding 071003, China. (e-mail: xiangwuy@ncepu.edu.cn)

Yanbo Wang, Qi Zhang and Zhe Chen are with the Department of Energy Technology, Aalborg University, Aalborg 9220, Denmark. (e-mail: ywa@et.aau.dk; qzg@et.aau.dk; zch@et.aau.dk)

I. INTRODUCTION

The application of renewable generation (RG), such as wind turbines (WT), significantly reduces carbon emissions of modern power system. However, new stability issues emerge in power grids with high penetration of RG, such as synchronization stability, sub-synchronous resonance, etc. [1], [2]. Unlike synchronous generators, the power electronic-interfaced RG exhibits different characteristics due to the control loop within a wide bandwidth range. Grid-following (GFL) control is an important control mode for RGs, which utilizes a phase-locked loop (PLL) to synchronize with the grid phase and output the power. This control structure is highly related to unstable phenomena within a wide frequency range due to the various timescales between control loops [3]. These unique stability problems require further analysis and discussion.

Small-signal analysis is an effective tool that linearizes the system at a certain operating point and performs stability analysis for small disturbances. For GFL-RG, the state-space models are established in [4]–[7], and impedance models are developed [8]–[10] to simplify the computation. In [4], the instability mechanism during low voltage ride-through is illustrated, which reveals that the interaction of the PLL and the current loop may lead to reduced system damping. To improve stability under fault conditions, in [5], a method for determining the PLL bandwidth is presented. Furthermore, in

[9], the PLL is considered to exhibit negative resistance characteristics primarily affecting low-frequency stability. The above studies show that the PLL dynamics are highly related to synchronization stability. Based on this consensus, the work in [11] analyzes the synchronization characteristics between PLL and grid, and quantifies the effect of different feedback channels. However, these studies mainly reveal the system's stability under small disturbances where the system is linearized at a certain operating point. However, the instability phenomenon in modern power systems with RG often happens in weak grids with longer durations [12], which causes the RG to deviate more from the operation point and results the system present a nonlinear characteristic.

Unlike small-signal analysis, transient analysis under large disturbances is performed directly based on nonlinear differential equations. Since higher-order differential equations cannot be solved analytically, three common methods are often employed for transient analysis, including numerical simulation, Lyapunov direct methods, and equal area criterion (EAC) method.

Numerical simulation methods are relatively straightforward for transient stability analysis since they usually rely on solving differential equations. In [13], an accurate time-domain model is established to assess the system stability under various control strategies. To identify key factors for transient stability, the model of RG is reduced and solved in the time domain in [14], [15]. However, numerical algorithms run slowly in large-scale simulations, and the most significant drawback is the lack of quantifiable stability criteria, which prevents the researchers from acquiring a physical concept and mechanism of transient stability.

The Lyapunov direct method is previously proposed to analyze and illustrate the stability boundary of a system by a well-established constructed energy function of the system. In [16], energy functions for GFL and grid-forming RG are constructed to compare their stability regions. The energy function is modified to ensure complete conservativeness in [17]. Nevertheless, the construction of energy function with minimal conservativeness is a significant challenge. Especially, the construction of the energy function mainly depends on experience in high-order systems, which makes it difficult to address stability issues in a form of general mathematical model.

Another effective solution for transient stability analysis is the EAC method [18]. In recent studies, the EAC method is employed in GFL-RG, which equivalents the system as a motion system and analyzes energy transfers. For example, the PLL is modeled as a second-order system similar to the rotor motion equation, and EAC is used for transient analysis in [19]. However, the analysis in [20] concludes that misjudgments may happen when using EAC that ignores the damping term. Then, it proposes a method to estimate maximum negative damping and ensure conservativeness. A discretized iterative method is further presented in [21] to eliminate the misjudgments but increases some computation. In summary, the computational accuracy and difficulty to estimate damping become contradictory. A modified EAC method that balances these two sides needs to be proposed.

Apart from PLL, power control also impacts transient stability in weak grid [22], which results in higher-order equations and makes it challenging to analyze with EAC methods. In the power control, the reactive power control supports the voltage stability of the power grid, and the active power control (APC) prevents the source side from DC overvoltage or rotor overspeed. In [23], reactive current control is modeled and analyzed to evaluate the transient stability during the low voltage ride-through process. In [24], a unified model of reactive power control is given to extend the stability analysis under different power control strategies. In [23] and [24], the effect of DC voltage control is considered, and the effect of APC on transient stability is analyzed. However, since the EAC method can only be applied in second-order systems, the above studies consider the power control as a proportional controller to avoid increased order or merely perform qualitative analysis.

To address aforementioned gaps, this paper combines the advantages of the clear mechanism in the EAC method and the high precision of discrete computations. Inspired by the work in [27], this article presents a motion discretization EAC (MD-EAC) method to calculate the effect of damping. Based on MD-EAC, a sequence mapping EAC (SM-EAC) method is further established to evaluate transient stability in the third-order system with power control. The main contributions of this paper are clarified as follows:

1) With a limited amount of calculation, the proposed MD-EAC method allows the damping energy to be considered analytically in each step, thus basically eliminating the error due to neglecting damping in the conventional EAC (CEAC) method.

2) The time sequence is obtained from the motion computation in the MD-EAC method. On this basis, the proposed SM-EAC method makes it possible to analyze the transient stability of third-order systems with power control.

3) The proposed SM-EAC method can evaluate possible multi-swing stability problems in GFL-DFIG. The integral parameter k_{ai} in APC is noted to be an important factor affecting multi-swing stability.

The rest of this paper is organized as follows. In Section II, a third-order transient model of the GFL-doubly fed induction generator (DFIG) is derived as an example of the GFL-WT. In Section III, an MD-EAC method is developed to solve the misjudgment in the CEAC method caused by damping. In addition, the power angle to time sequence is established to estimate the output of the APC. The MD-EAC and the sequence mapping together form the SM-EAC method. In Section IV, simulation is given to validate the effectiveness of MD-EAC and SM-EAC. Also, the phenomenon of multi-swing instability is found and analyzed in GFL-DFIG. The conclusions are drawn in Section V.

II. Transient Modeling of GFL-DFIG

A. *Modeling of DFIG and PLL*

The stator of GFL-DFIG is directly connected to the point of common coupling (PCC) through line impedance. The grid side converter (GSC) ensures a constant voltage on the DC bus, while the rotor side converter (RSC) controls the stator

output current to follow the grid phase generated by PLL. The reference current values of RSC are from the power control loop, where the APC generates the active current I_{rd}, and the reactive current is constant as I_{ms} in unit power factor operation. Pitch control is used to adjust the blade angle β to control the input torque. The block diagram of GFL-DFIG system with control loops is shown in Fig. 1. According to the winding turns, the rotor side quantities above are converted to the stator side. All reactance values are calculated in the rated frequency f.

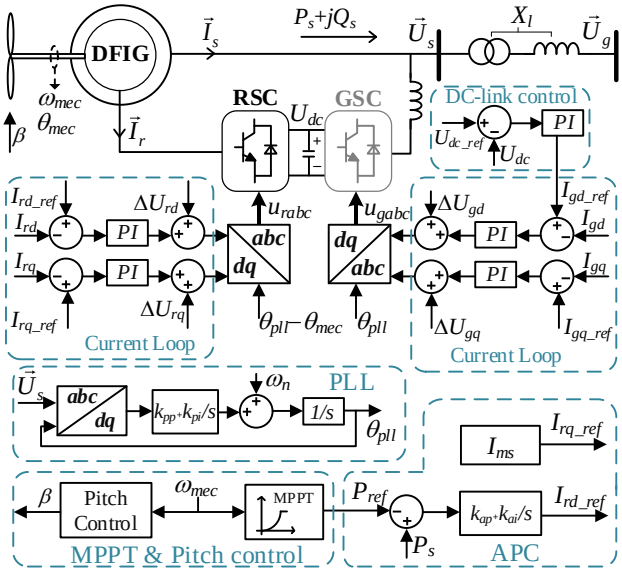

Fig. 1. Block diagram of GFL-DFIG system with control loops.

Before the transient stability analysis, the relevant simplifications and conditions are clarified as follows.

1) For the large renewable power system, the resistance of the system is ignored. Besides, since the output current frequency of the GFL-DFIG does not significantly change the grid reactance, the reactance is calculated only at the rated frequency f [14]. In fact, if the analysis object is the converter, the consideration of the reactance change due to frequency mutation does not affect the model's order but only changes the coefficients of the equation [21].

2) The transient overcurrent and overvoltage protection process is ignored, since this duration is often less than 50ms [28] and barely affects the transient synchronization stability.

3) Unlike the transient work between PLL and current loop in [29], this study focuses on the transient stability affected by the APC and PLL parts, which are slower compared to the current loop. Therefore, the current loop dynamics could be ignored, i.e., I_{rdq}=I_{rdq_ref}.

4) The dynamic of the GSC is neglected because it occupies a small capacity and shares the same PLL with the RSC.

In DFIG, the rotor current phase and the mechanical angle are superimposed to build the synthetic magnetic field. The generated voltage on the stator lags the synthetic magnetic field by $\pi/2$. Therefore, the generated voltage on the stator of the DFIG during the transient process is given as (1).

$$\vec{E}_s = -j\omega_s L_m \vec{I}_r e^{j\theta_{mec}} = -jX_m \vec{I}_r e^{j\theta_{mec}} \quad (1)$$

In the current loop of GFL-DFIG, the rotor current is decomposed by the difference between θ_{pll} and θ_{mec}:

$$[I_{rd}\ \ I_{rq}]^T = \mathbf{P}(\theta_{pll} - \theta_{mec})\vec{I}_r \quad (2)$$

Extracting θ_{mec} from $\mathbf{P}$, we can obtain:

$$[I_{rd}\ \ I_{rq}]^T = \mathbf{P}(\theta_{pll})\vec{I}_r e^{j\theta_{mec}} \quad (3)$$

where θ_{rdq} is defined as:

$$\theta_{rdq} = \arctan(\frac{I_{rq}}{I_{rd}}) \quad (4)$$

The generated voltage on the stator can be calculated as (5) by combining (1) and (3).

$$\vec{E}_s = -jX_m(I_{rd} + jI_{rq})e^{j\theta_{pll}} \quad (5)$$

The DFIG connects to the PCC via the line reactance, and the circuit equation of the system can be established as (6).

$$\vec{U}_g = \vec{E}_s - jX_s\vec{I}_s - jX_l\vec{I}_s \quad (6)$$

From (6), the circuit diagram and phase diagram of DFIG are shown in Fig. 2.

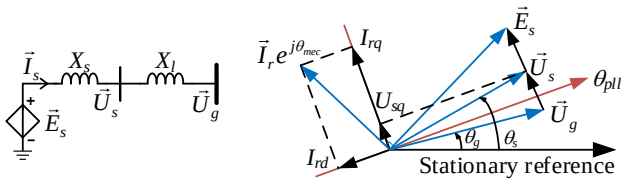

Fig. 2. The transient model of GFL-DFIG. (a) circuit, (b) phase diagram.

From Fig. 2(b), the input of the PLL U_{sq} can be derived as:

$$U_{sq} = \mathrm{Im}[\vec{U}_s e^{-j\theta_{pll}}] = (1-a)U_g \sin(\theta_g - \theta_{pll}) - aX_m I_{rd} \quad (7)$$

where,

$$a = \frac{X_l}{X_l + X_s} \quad (8)$$

The differential equation of PLL in Fig. 1 is given as:

$$\theta_{pll} = \frac{1}{s}[(k_{pp} + \frac{k_{pi}}{s})U_{sq} + \omega_n] \quad (9)$$

Substituting (7) into (9), we can obtain the second-order nonlinear equations of PLL as:

$$\ddot{\delta} + k_{pp}(1-a)U_g \cos\delta\dot{\delta} = -k_{pi}aX_m I_{rd} - k_{pi}(1-a)U_g \sin\delta \quad (10)$$

where the power angle δ is defined as:

$$\delta = \theta_{pll} - \theta_g \quad (11)$$

The velocity ω is the differential of the power angle δ:

$$\omega = \dot{\delta} \quad (12)$$

Equations (10) and (12) construct a second-order motion system, which determines the transient characteristic of DFIG and PLL in GFL control.

B. Modeling of APC

For GFL-RG, the APC is an essential part in the transient process since the safety of the renewable energy source relies on the APC. For instance, during the transient process of a DFIG, it should still output a certain power to prevent the

rotor overspeed. In addition, APC provides sufficient active power support to the power grid, preventing other problems like low-frequency load shedding. The general form of the APC is given as:

$$I_{rd\_ref} = -(k_{ap} + \frac{k_{ai}}{s})(P_{ref} - P_s) \tag{13}$$

(13) is a first-order differential equation. The stator power in (13) can be calculated from (5) and (6).

$$\begin{aligned} P_s &= \frac{I_r X_m U_g}{X_s + X_l} \sin(\theta_{pll} + \theta_{rdq} - \frac{\pi}{2} - \theta_g) \\ &= \frac{X_m U_g}{X_s + X_l}(I_{rq} \sin\delta - I_{rd} \cos\delta) \end{aligned} \tag{14}$$

Due to the application of APC, the GFL-DFIG becomes a third-order nonlinear system consisting of (10), (12) and (13).

III. Transient Stability Analysis

This section first shows the CEAC method and investigates its limitations. Furthermore, to solve the misjudgment in CEAC method, the MD-EAC method is proposed to correct the non-Hamiltonian damping component. Finally, the SM-EAC method is applied to the third-order system by the proposed sequence mapping.

A. CEAC Method

Neglecting the effect of APC on I_{rd}, for the second-order system defined by (10), it can be multiplied by $\dot{\delta}$ and then integrated over t for both sides:

$$\begin{aligned} &\int \ddot{\delta}\dot{\delta}dt + \int k_{pp}(1-a)U_g \cos\delta\dot{\delta}d\delta \\ &= \int (-k_{pi}aX_m I_{rd} - k_{pi}(1-a)U_g \sin\delta)d\delta \end{aligned} \tag{15}$$

For the sake of uniform formatting, ω is not used in (15) to replace $\dot{\delta}$. (15) represents the energy equation in a second-order system, which satisfies energy conservation:

$$E_k + E_p + E_d = 0 \tag{16}$$

E_k, E_p, and E_d can be defined and simplified as:

$$\begin{cases} E_k = \int \ddot{\delta}\dot{\delta}dt = \int \dot{\delta}d\dot{\delta} = \frac{1}{2}\dot{\delta}^2 = \frac{1}{2}\omega^2 \\ E_p = \int (k_{pi}aX_m I_{rd} + k_{pi}(1-a)U_g \sin\delta)d\delta \\ \quad = k_{pi}aX_m I_{rd}\,\delta - k_{pi}(1-a)U_g \cos\delta \\ E_d = \int k_{pp}(1-a)U_g \cos\delta\dot{\delta}d\delta = \int k_{pp}(1-a)U_g \cos\delta\omega d\delta \end{cases} \tag{17}$$

Similar to the synchronous generator, we can find P_{em}, P_{ee} and P_{ed} as:

$$\begin{cases} P_{em} = -k_{pi}aX_m I_{rd} \\ P_{ee} = k_{pi}(1-a)U_g \sin\delta \\ P_{ed} = k_{pp}\omega(1-a)U_g \cos\delta \end{cases} \tag{18}$$

(18) characterizes a rotating system which is driven by P_{em}, restrained by P_{ee} and damped by P_{ed}. As shown in Fig. 3, The intersection of P_{em} and P_{ee} on the left and right are stable equilibrium point (SEP) and unstable equilibrium point (UEP), respectively. The second-order system can be analyzed using the CEAC method to obtain a stability criterion S for the system:

$$S = \int_{\delta_0}^{\delta_{UEP}} P_{em} - P_{ee} - P_{ed}\,d\delta \tag{19}$$

where δ_0 is the starting point in the transient process, and δ_{UEP} is the position of UEP. Neglecting P_{ed}, S can be solved analytically. When $S \leqslant 0$, the system is asymptotically stable; when $S>0$, the system is unstable in the transient process.

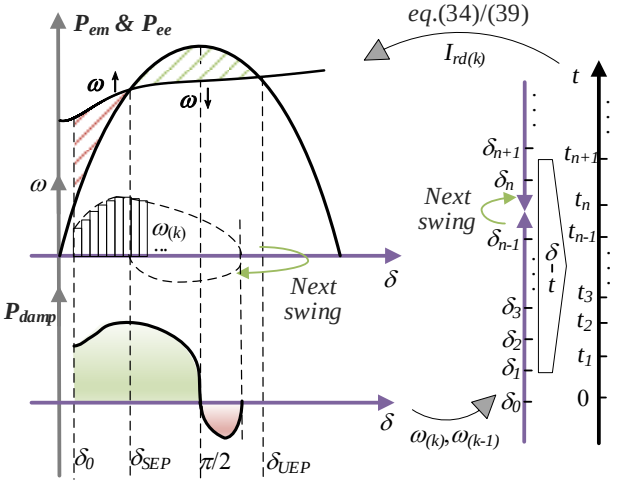

Fig. 3. SM-EAC with MD-EAC and sequence mapping part.

The CEAC method is based on the synchronous generator, which always has a positive damping power [18]. Hence, CEAC is conservative to the synchronous generator when neglecting damping. However, in GFL-DFIG, the cosine component of P_{ed} in (18) causes the damping negative on the right side of $\pi/2$. This uncertainty regarding the damping component leads to either aggressive or conservative misjudgments about the system's stability, as mentioned in [17], [21].

B. MD-EAC Method

The system containing the P_{ed} and ω is a non-Hamiltonian system, which indicates that when the trajectory moves to a certain position at different moments, the power is determined not only by the position, but also by the different velocities. Consequently, to accurately analyze transient processes in such systems, it is necessary to determine ω in the motion.

To determine ω and P_{ed}, we can first discrete the motion by the step size δ_{step}. A recursive algorithm then calculates the velocity ω_k at the kth step, and the ω_k can be used to forecast the damping in the next step.

In order to implement the above algorithm, the initial velocity should first be determined. $\omega_{(0-)}$ and $\omega_{(0+)}$ are the velocities before and after the disturbance, respectively, and they can be calculated from (9), (11) and (12):

$$\begin{cases} \omega_{(0-)} = k_{pp}U_{sq(0-)} + \int_0^{t_{0-}} k_{pi}U_{sq}dt \\ \omega_{(0+)} = k_{pp}U_{sq(0+)} + \int_0^{t_{0+}} k_{pi}U_{sq}dt \end{cases} \tag{20}$$

Since the integral does not abrupt at the disturbance moment, $\omega_{(0+)}$ can be derived from the output of the proportion

part:

$$\omega_{(0+)}=\omega_{(0-)}-k_{pp}(1-a)\sin\delta_0(U_{g(0+)}-U_{g(0-)}) \tag{21}$$

After calculating $\omega_{(0+)}$, the velocity from the beginning to the first step δ_1 can be considered as $\omega_{(0+)}$ and calculate the P_{ed}.

$$P_{ed(0+,1)}=k_{pp}\omega_{(0+)}(1-a)U_g\cos\delta \tag{22}$$

Thus, the change of kinetic energy in this step and the new velocity in the next step can be represented as (23)-(25).

$$\begin{aligned}\Delta E_{k(0+,1)}&=\int_{\delta_0}^{\delta_1}P_{em}-P_{ee}-P_{ed(0+,1)}dt\\&=E_p\big|_{\delta_0}^{\delta_1}-k_{pp}\omega_{(0+)}(1-a)U_g\sin\delta\big|_{\delta_0}^{\delta_1}\end{aligned} \tag{23}$$

$$E_{k(1)}=\frac{1}{2}\omega_{(0+)}^2+\Delta E_{k(0+,1)} \tag{24}$$

$$\omega_{(1)}=\sqrt{E_{k(1)}} \tag{25}$$

where the integral in (23) can be calculated analytically. For subsequent steps, we can substitute 0+ and 1 with the step numbers *k-1* and *k* in the recursive MD-EAC.

If $E_{k(n)}<0$ in (25), it indicates that the power angle at δ_{n-1} is already close to the first-swing endpoint (FEP). Subsequently, it reaches the FEP, then returns to the position of δ_{n-1}. This process completes the first swing and enters the second swing. In these two stages, due to the reversal of the integral limits on the δ-axis, the original driving force and resistance transform into each other. Therefore, the motion process is symmetrical in these two stages, and the initial velocity of the second swing is given as (26).

$$\omega_{(n)}=-\omega_{(n-1)} \tag{26}$$

With the initial velocity known as (26), the transient process in the second swing can be calculated by repeating (23)-(25). Similarly, the analysis in the muti-swing process can be performed.

The application of the MD-EAC is shown in Fig. 3. It is important to note that the power transfer in EAC is rigorous, and the error here is from the approximation for ω. Besides, the dynamic of PLL is much faster than that of APC [30], [31], which means the variation of I_{rd} is tiny within one step. Therefore, the equations of the PLL do not include differentiation of I_{rd}. To minimize the precision loss, the linearized slope of I_{rd} or a well-selected interpolation method can be introduced to enhance MD-EAC. However, the accuracy improvements with these methods are limited due to the separated timescales, especially when the step is small.

C. MD-EAC Method Applied to Multi-DFIG Parallel System

We also investigate the MD-EAC method's applicability in multi-DFIG parallel systems. In an actual multi-DFIG parallel system, each DFIG operates under distinct wind speeds and line reactance conditions. Fig. 4 shows the diagram of the multi-DFIG parallel system.

The voltage equation for the system in Fig. 4 is given as (27).

$$\begin{bmatrix}\vec{I}_1\\ \vdots\\ \vec{I}_n\\ 0\\ \vec{I}_g\end{bmatrix}=\begin{bmatrix}y_{t1} & & & -y_{t1} & 0\\ & \ddots & & \vdots & \vdots\\ & & y_{tn} & -y_{tn} & 0\\ -y_{t1} & \cdots & -y_{tn} & y_\Sigma & -y_l\\ 0 & \cdots & 0 & y_l & -y_l\end{bmatrix}\begin{bmatrix}\vec{E}_1\\ \vdots\\ \vec{E}_n\\ \vec{U}_{bus}\\ \vec{U}_g\end{bmatrix} \tag{27}$$

where $\vec{E}_i$ and $\vec{I}_i$ represent the generated voltage and output current of the DFIG$_i$, $\vec{U}_{bus}$ is the bus voltage of the wind farm, y_{ti} is the line admittance of DFIG$_i$, and y_Σ represents the self-admittance of the bus.

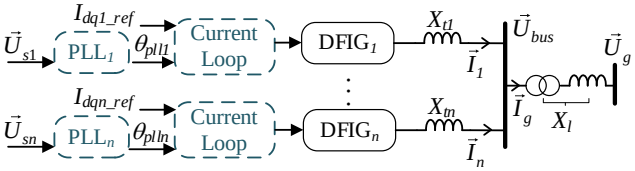

Fig. 4. The diagram of multi-DFIG parallel system.

The DFIG$_i$'s stator voltage $\vec{U}_{si}$ is given as (28).

$$\vec{U}_{si}=\vec{U}_g-jX_l\vec{I}_g-jX_l\vec{I}_i \tag{28}$$

Substituting the current obtained from (27), we can obtain the structure of $\vec{U}_{si}$:

$$\vec{U}_{si}=\sum_{j=1}^{n}A_j\vec{E}_j+B\vec{U}_g \tag{29}$$

in which, A and B are the constants defined by (27). As the input of PLL$_i$, U_{sqi} is:

$$\begin{aligned}U_{sqi}=&\sum_{\substack{j=1\\ j\neq i}}^{n}A_jX_m[I_{rqj}\sin(\theta_{pllj}-\theta_{plli})-I_{rdj}\cos(\theta_{pllj}-\theta_{plli})]\\&+BU_g\sin(\theta_g-\theta_{plli})-A_iX_mI_{rdi}\end{aligned} \tag{30}$$

Then, the nonlinear equation of PLL$_i$ can be established as:

$$\ddot{\delta}_{plli}=P_{emi}-P_{eei}-P_{edi} \tag{31}$$

in which,

$$\begin{cases}P_{emi}=-k_{pi}A_iX_mI_{rdi}\\ P_{eei}=k_{pi}\left\{BU_g\sin\delta_{plli}-X_m\sum\limits_{\substack{j=1\\ j\neq i}}^{n}A_j\begin{bmatrix}I_{rqj}\sin(\delta_{pllj}-\delta_{plli})\\ -I_{rdj}\cos(\delta_{pllj}-\delta_{plli})\end{bmatrix}\right\}\\ P_{edi}=-k_{pp}\left\{\begin{matrix}-BU_g\cos\delta_{plli}\dot{\delta}_{plli}\\ +X_m\sum\limits_{\substack{j=1\\ j\neq i}}^{n}A_j\begin{bmatrix}I_{rqj}\cos(\delta_{pllj}-\delta_{plli})(\dot{\delta}_{pllj}-\dot{\delta}_{plli})\\ +I_{rdj}\sin(\delta_{pllj}-\delta_{plli})(\dot{\delta}_{pllj}-\dot{\delta}_{plli})\end{bmatrix}\end{matrix}\right\}\end{cases} \tag{32}$$

δ_{plli} is defined as the power angle for the DFIG$_i$. For a wind farm containing n identical DFIGs, the power angle and its velocity of the equivalent swing center [32] can be defined as the average value of DFIGs:

$$\delta_o=\sum_{j=1}^{n}\delta_j/n \tag{33}$$

$$\omega_o = \sum_{j=1}^{n} \omega_j / n \tag{34}$$

For the swing center, its second-order equation can be derived by superposing the nonlinear equations of the DFIG units as (35).

$$\ddot{\delta}_o = \frac{1}{n}\sum_{i=1}^{n}(P_{emi} - P_{eei} - P_{edi}) \tag{35}$$

Since swing center represents the external characteristics of the DFIG cluster, the relative motion within the cluster in (35) can be neglected, which makes the swing-center equation similar to the single-machine equation. The introduction of the swing center reduces the order of multi-DFIG parallel system and enables the analysis through MD-EAC.

D. Power Angle to Time Sequence Mapping

The challenge in applying EAC to a third-order system is that all energy calculations within CEAC are conducted in the power angle domain, whereas APC dynamic as (13) is in time-domain. Therefore, it is important to establish the relation between the power angle and time in the third-order system. In the MD-EAC process, we discretize the system dynamics into equidistant points along the δ-axis. If the time sequence can be established corresponding to the δ-axis, then APC in the third-order system could be considered and computed at each δ.

As the system moves from δ_{k-1} to δ_k, the average value of velocity is:

$$\bar{\omega}_{(k-1,k)} = \frac{\omega_{(k-1)} + \omega_{(k)}}{2} \tag{36}$$

If $\bar{\omega}_{(k-1,k)}$ is regarded as the average velocity of this displacement, the time passed in this displacement is:

$$\Delta t_{(k-1,k)} = \frac{\delta_{step}}{\bar{\omega}_{(k-1,k)}} \tag{37}$$

Then, we can obtain the time sequence at step k, as:

$$t_{(k)} = \sum_{i=0}^{k} \Delta t_{(i-1,i)} \tag{38}$$

For the δ_{n-1} close to FEP and the δ_n in the next swing, the duration between them can be defined as:

$$\Delta t_{(n-1,n)} = \frac{2\omega_{(n-1)}}{(\omega_{(n-2)} - \omega_{(n-1)})/\delta_{step}} \div \frac{\omega_{(n-1)}}{2} = \frac{\delta_{step}}{\omega_{(n-2)} - \omega_{(n-1)}} \tag{39}$$

The implication of (39) is to linearize the process from δ_{n-1} to FEP in the phase plane as the same slope from δ_{n-2} to δ_{n-1}, and then consider the velocity of this displacement as the average of $\omega_{(n-1)}$ and 0. In the calculation with a smaller step, since δ_{n-1} and FEP are close, the time duration between these two points could be set to 0. In the next swing, repeating (36)-(38) yields a new power angle to time sequence, as shown in Fig.3.

E. APC in Time Sequence

The dynamics of the APC can be obtained in a discrete sequence. In the initialization process, the mutation in the APC's proportion part needs to be taken into account. From (13) and (14), $I_{rd(0+)}$ can be solved as:

$$\begin{aligned} I_{rd(0+)} = \frac{-k_{ap}}{1+k_{ap}b\cos\delta_0 U_{g(0+)}}[&I_{rq}b\sin\delta_0(U_{g(0-)} - U_{g(0+)}) \\ &+(-\frac{1}{k_{ap}} - b\sin\delta_0 U_{g(0-)})I_{rd(0-)})] \end{aligned} \tag{40}$$

where,

$$b = \frac{X_m}{X_s + X_l} \tag{41}$$

At each of the following points in the time sequence, $I_{rd(k)}$ could be calculated by two methods:

1) Incremental Method

The increments of the PI controller output can be expressed by proportion and integral in the step. Therefore, the relationship between $I_{rd(k-1)}$ and $I_{rd(k)}$ can be calculated as:

$$\begin{aligned} I_{rd(k)} &= I_{rd(k-1)} + \Delta I_{rd(k-1,k)} \\ &= I_{rd(k-1)} - k_{ap}(P_{s(k-1)} - P_{s(k)}) - k_{ai}\Delta t_{(k-1,k)}(P_{ref} - P_{s(k-1)}) \end{aligned} \tag{42}$$

where $I_{rd(k)}$ is included in the $P_{s(k)}$. When $P_{s(k)}$ is rewritten with $I_{rd(k-1)}$ and $\Delta I_{rd(k-1,k)}$, $\Delta I_{rd(k-1,k)}$ can be solved as:

$$\begin{aligned} \Delta I_{rd(k-1,k)} = \frac{-1}{1+k_{ap}bU_g\cos\delta_k}\{&k_{ai}\Delta t_{(k-1,k)}(P_{ref} - P_{s(k-1)}) \\ &+k_{ap}[P_{s(k-1)} - bU_g(I_{rq}\sin\delta_k - I_{rd(k-1)}\sin\delta_k)]\} \end{aligned} \tag{43}$$

2) Exponential Fitting Method

Taking the derivatives on both sides of (13) and neglecting the current loop dynamic, it can be obtained:

$$\dot{I}_{rd} = k_{ap}\dot{P}_s - k_{ai}(P_{ref} - P_s) \tag{44}$$

The DFIG operates at unit power factor mode, therefore the differentiation of I_{rq} can be neglected, and $\dot{P}_s$ is

$$\dot{P}_s = \frac{X_m U_g}{X_s + X_l}(I_{rq}\omega\cos\delta + \omega I_{rd}\sin\delta - \dot{I}_{rd}\cos\delta) \tag{45}$$

Substituting $\dot{P}_s$, (44) can be rewritten into a differential equation as:

$$A\dot{I}_{rd} + BI_{rd} = C \tag{46}$$

where,

$$\begin{cases} A = 1 + k_{ap}U_g b\cos\delta \\ B = -k_{ap}U_g b\omega\sin\delta + k_{ai}U_g b\cos\delta \\ C = k_{ap}U_g b\omega I_{rq}\cos\delta - k_{ai}P_{ref} + k_{ai}bI_{rq}\sin\delta \end{cases} \tag{47}$$

Then I_{rd} can be solved as:

$$I_{rd} = k_I e^{-\frac{B}{A}t} + \frac{B}{C} \tag{48}$$

$A_{(k-1)}$, $B_{(k-1)}$, and $C_{(k-1)}$ are all directly calculated algebraically at δ_k, and the coefficient $k_{I(k-1)}$ is also directly solved as:

$$k_{I(k-1)} = \frac{I_{rd(k-1)} - \left(B_{(k-1)} \middle/ C_{(k-1)}\right)}{e^{-\frac{B_{(k-1)}}{A_{(k-1)}}t_{(k-1)}}} \tag{49}$$

Now (48) turns into a time function, and $I_{rd(k)}$ in the next step can be forecasted as:

$$I_{rd(k)} = k_{I(k-1)} e^{-\frac{B_{(k-1)}}{A_{(k-1)}} t_{(k+1)}} + \frac{B_{(k-1)}}{C_{(k-1)}} \tag{50}$$

After determining the calculation method of I_{rd} in the initial and each step next, the I_{rd} in the whole transient process is known entirely, which can be calculated and applied step by step. The difference between the two methods is that the exponential method performs the differentiation of P_s in (46), which means that the dynamic of P_s is estimated in this step. However, the incremental method considers the error integral as an accumulation of the error at point δ_k.

Two aforementioned APC calculation methods above exhibit a similar feedback negative mechanism: in calculating the $I_{rd(k)}$, the methods consider the input as the error generated by the $I_{rd(k-1)}$, so that the error input of the algorithm is higher than of actual error. Subsequently, the methods yield an I_{rd} output slightly greater than the actual in that step. Then, in the next step, the accumulated error in the previous step decreases I_{rd}. Therefore, no static error is accumulated and amplified in the algorithm of I_{rd}. This algorithm enhances accuracy in long-time-lasting and multi-swing analysis.

F. SM-EAC Method

For the transient process, the response of the APC is much slower than that of the PLL [30], [31], which means the variation of I_{rd} is tiny within one step of δ. Therefore, in the previous analysis, the slow dynamic of I_{rd} is ignored in the MD-EAC calculation, while the rapid changes in power angle are considered through the exponential fitting method incorporating the velocity of power angle. Such an approach achieves a trade-off between algorithmic complexity and accuracy. To summarize and apply the above methods to a third-order system, we consider I_{rd} as constant to use MD-EAC method in each step and perform the power angle to time mapping after this step. Then, a new I_{rd} is generated for the MD-EAC calculation in the next step. This alternating approach between the δ-domain and time domain is named SM-EAC, whose computational loop contains MD-EAC and sequence mapping is illustrated in Fig .3. The flowchart of SM-EAC is depicted in Fig. 5 to provide a clear representation of the computational structure between parts.

For RG systems, the droop control of reactive current and current saturation may cause a decrease in P_{em} in a larger power angle region, resulting in a rightward shift of the UEP [23]. In various reactive droop modes, the curve of P_{em} differs but remains greater than 0, which means that the UEP is always less than π. Therefore, in Fig. 5, the criterion for judging the system instability is set as $\delta_k > \pi$. For the stable condition, in this paper, the judgment is set to be $\omega_k < |\omega_{\min}|$, which indicates the phase trajectory is stabilized on the x-axis.

While retaining the advantages of the clear mechanism in EAC method, the proposed SM-EAC introduces APC through sequence mapping, which makes it applicable to third-order systems. Its alternating computation between the time domain and the δ domain utilizes the concept of partial linearization in a dynamic process. In SM-EAC, the effects of damping and APC are algebraically computed before and after each step with the discrete EAC method, which avoids additional integration loops or iteration calculations. In fact, SM-EAC runs the same number of steps as one loop calculation in the relative iterative method [21]. Compared to previous iterative methods, SM-EAC significantly enhances operational speed, which makes it highly valuable for engineering applications.

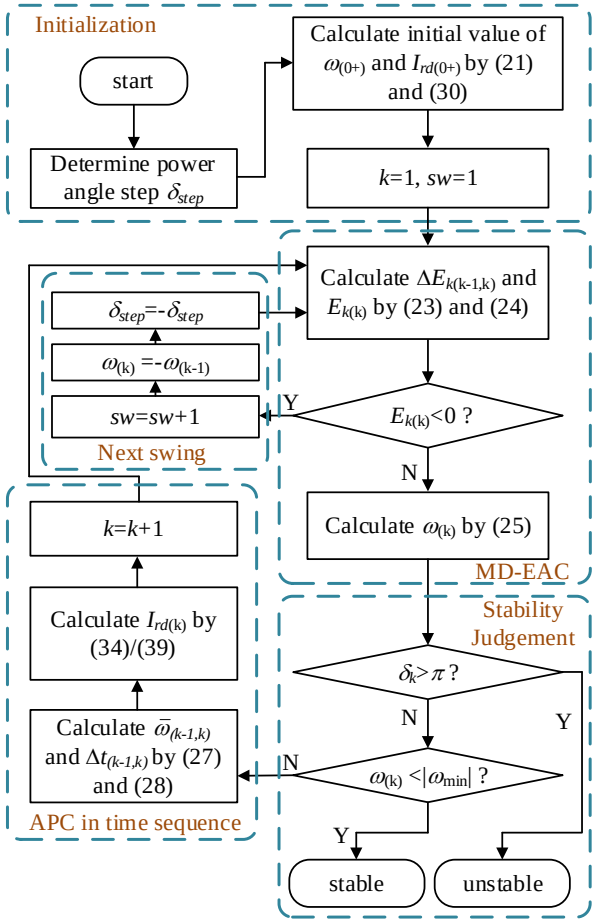

Fig. 5. Computational flowchart of proposed SM-EAC.

IV. Simulation Verification and Analysis

In this section, as the basis of SM-EAC, the accuracy of the MD-EAC is first validated in various conditions. Subsequently, we analyze the SM-EAC method's effectiveness and potential inaccuracy. Finally, the proposed SM-EAC is used for the evaluation and analysis of multi-swing stability.

A. Accuracy of MD-EAC

Firstly, a single machine infinite bus (SMIB) is employed for validation, in which a detailed model aggregated with 6 DFIGs connects to the infinity bus through the line. The parameters of DFIGs are listed in Table I in the Appendix.

The objective of this part is to validate the effectiveness of MD-EAC in second-order systems. Therefore, the APC is not introduced, I_{rd} and I_{rq} are set as constant values of -0.69 pu and 0.26 pu respectively in this part. In the discrete transient calculations, the step size is selected as 1×10^{-3} rad.

In order to demonstrate that the conservative or aggressive problems of CEAC are modified by MD-EAC, two cases are introduced as follows.

Case 1: The PCC suffers a permanent fault, resulting in a voltage drop of 0.5 pu. The line reactance is 0.6 pu.

Case 2: The line reactance is the same as case 1. The PCC suffers a voltage drop of 0.8 pu for 400 ms, and then the PCC voltage is restored to 1 pu.

As shown in Fig. 6, different stable boundaries and trajectories are drawn under the CEAC and MD-EAC. The actual simulation results under the two cases are also shown in Fig. 6.

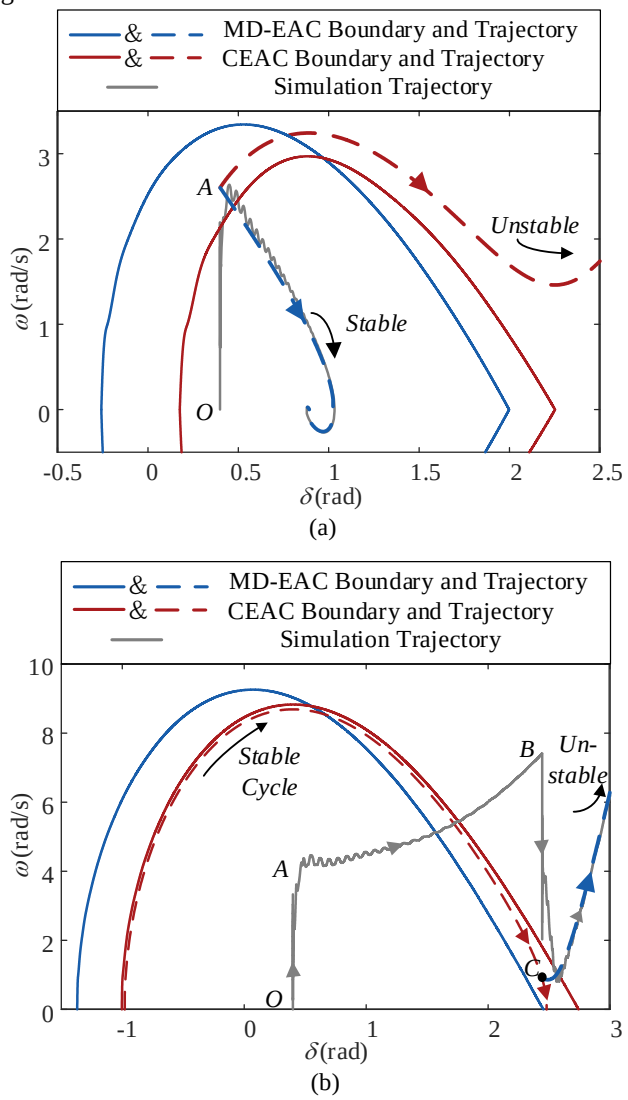

Fig. 6. GFL-DFIG's transient boundaries and trajectories in simulation and different methods. (a) Case 1. (b) Case 2.

The line segment OA in Fig. 6(a) represents the velocity mutation at the moment of the voltage drop. Point A is the starting point of MD-EAC and CEAC calculation, and its vertical coordinate $\omega_{(0+)}$ is obtained by initializing the equation (21). Point A is located at the intersection of the CEAC instability region and the MD-EAC stability region, which could obtain different transient stability results to compare the effectiveness of the methods. In this case, when the majority of the post-disturbance trajectory is within the positively damped region, the CEAC method fails to determine the system's stability and reflects conservatism due to insufficient estimation of positive damping. However, when applying the MD-EAC method, the system has more resistance force than the previous CEAC estimation because the positive damping is properly considered. Therefore, the transient and actual trajectory are consistently stable and almost converge at the same point in the phase plane, which verifies the effectiveness of MD- EAC.

The OA and AB processes in Fig. 6(b) represent the stage from the voltage drop to the end of the drop after 400ms, during which MD-EAC and CEAC yield consistent stability assessments. For simplicity, the trajectories obtained by both EAC methods during this stage are not depicted in Fig.6(b). After that, the line segment BC is the voltage recovery moment. Point C is the starting point for both methods, and it is critical since it lies in the intersection of the MD-EAC instability region and the CEAC stability region. For the stability of the system after Point C, the MD-EAC method aligns with the actual trajectory and tends towards instability, while the CEAC method makes a misjudgment, which validates the effectiveness of MD-EAC in case 2. So, MD-EAC solves the aggressive problem of CEAC. The contrasting judgment results occur due to the CEAC method's oversight of damping effects when the post-disturbance trajectory largely exists within the negatively damped region. This oversight leads to underestimating acceleration energy, allowing for a stable cycle without adequate energy dissipation. By contrast, the MD-EAC method estimates the negative damping, which is a part of the actual driving force in the system. Therefore, the calculated unstable trajectory nearly matches the same as the actual trajectory.

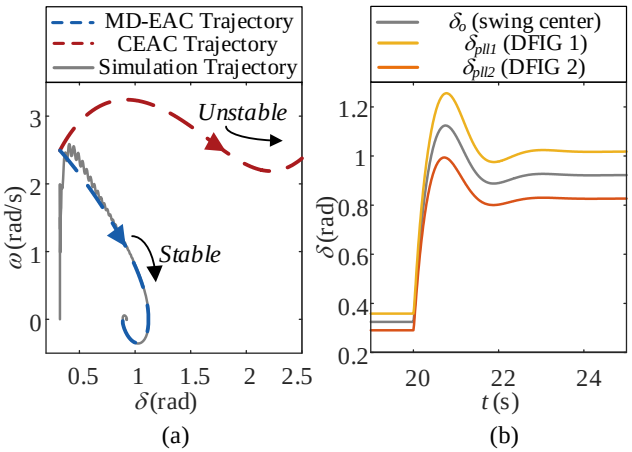

Fig. 7. Transient process of two-DFIG parallel system. (a) Phase trajectories in simulation and different methods. (b) Power angles under time domain in simulation.

To verify the applicability of MD-EAC in a multi-DFIG parallel system, we select a two-DFIG parallel system, where each DFIG is aggregated from 3*1.5 MW DFIG units. Due to the different locations of DFIGs, they present different I_{rd} and

line reactance to the bus, and the system parameters are shown in Table II in the Appendix. The fault is a 0.6 pu permanent drop voltage in the U_g at 20s. The trajectories of CEAC, MD-EAC and actual simulation are shown in Fig. 7(a), and the time domain waveforms of the power angle for each unit and swing center are shown in Fig. 7(b).

As shown in Fig. 7(a), MD-EAC successfully estimates the transient trajectory of the system and effectively judges the stability of the parallel DFIG system. However, CEAC misjudges the system as unstable. Fig. 7(b) shows that the power angle of the swing center is always in sync with the parallel DFIG unit, which proves the reasonableness of using the swing center to judge the transient stability of the parallel DFIG.

B. Effectiveness of SM-EAC

In the validation part of SM-EAC method, DFIG with the same parameters as Table I is selected. The line impedance in the SMIB system is 0.45 pu. The detailed model with APC is introduced in simulation, and its parameters are set as k_{ap}=3 and k_{ai}=0.6 according to [33]. The SM-EAC methods using both incremental and exponential fitting methods are validated. The previous EAC method, which only considers proportional controllers as [21] and [23], is used as a comparison. Besides, we employ the MD-EAC to calculate the damping in the previous method to conduct the comparison. To improve the accuracy of this proportional MD-EAC method, we consider the effect of the initial value of the integral as:

$$I_{rd\_ref} = x_0 - k_{ap}(P_{ref} - P_s) \tag{51}$$

where x_0 is the output of the integrator of the PI controller before the fault. Therefore, (51) considers the controller as a PI before disturbance and then degrades to a proportional controller during the transient process. This change allows the system to operate without static error during normal operation and solves the problem of inconsistency between previous studies and actual operation.

Case 1, case 2, and case 3 suffered permanent voltage drops of 0.2, 0.3, and 0.35 pu to demonstrate stability under different conditions, respectively. The 3D trajectories with I_{rd} as z-axis and phase trajectories are shown in Fig. 8.

In Fig. 8(a), all three methods evaluate that the system is stable. However, since the proportional MD-EAC method does not consider the integration of error, δ stops at about 0.47, where I_{rd} is about -0.86. The two proposed SM-EAC methods coincide with the actual trajectory. Finally, δ stops at about 0.54, where I_{rd} is about -0.97.

In Fig. 8(b), the proportional MD-EAC method evaluates that the system is stable, which is inconsistent with the actual situation. In fact, the system becomes unstable after entering the third swing. The proposed SM-EAC methods accurately predict the instability in the third swing. However, in the region with a larger power angle, the proposed methods show some deviation compared to the actual trajectory, particularly

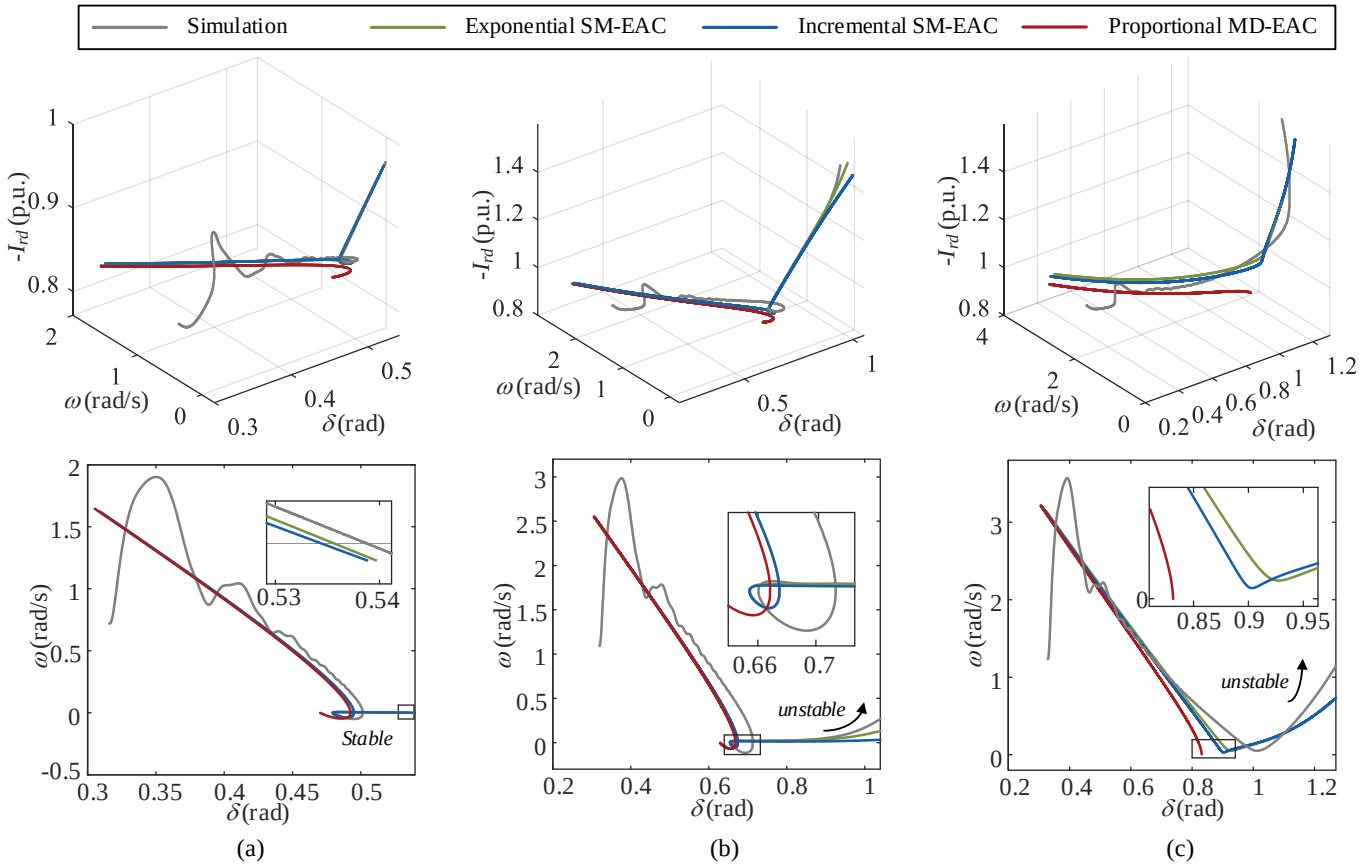

Fig. 8. 3D trajectories and plane trajectories in simulation and different methods. (a) Case 1. (b) Case 2. (c) Case 3.

the incremental SM-EAC method. This might be attributed to slow velocities but rapid accelerations during this condition, which causes a certain delay in the proposed methods. Nevertheless, the unstable phenomenon can be determined by calculating the acceleration/deceleration energy and the existence of SEP before entering the error region. SM-EAC remains effective in transient stability analysis.

Fig. 8(c) is a more critical scenario, which reveals the instability phenomenon that occurs at the velocity very close to 0 in the first swing. For the proportional MD-EAC method, the absence of APC's integration in the first swing leads to the incorrect stability judgment. On the other hand, the two proposed methods successfully estimate the integral output and indicate system instability. Similar to case 2, there are also some deviations in the zone with lower velocities, but these do not affect the final result.

To demonstrate the accuracy of the power angle to time sequence mapping, the time-domain waveforms about calculation variables in case 2 are shown in Fig. 9(a). Besides, important variables not included in the calculation are shown in Fig. 9(b).

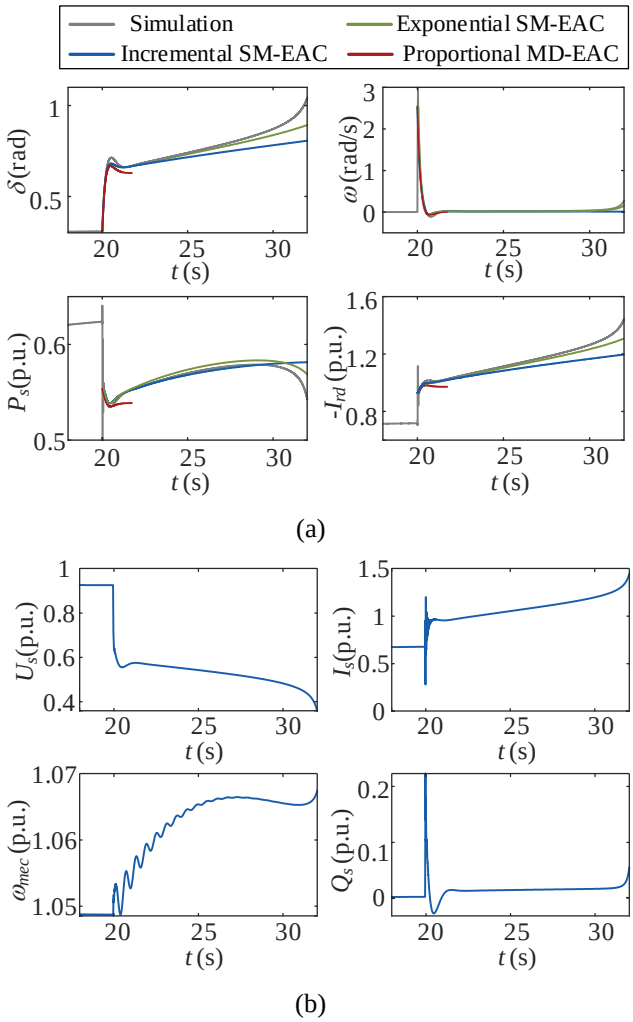

Fig. 9. GFL-DFIG's transient waveforms. (a) Calculation variables in simulation and different methods; (b) Important variables in the simulation.

As shown in Fig. 9(a), in the first swing, all three methods reasonably estimate the maximum power angle. Subsequently, due to the misjudgment of stability, the proportional MD-EAC stops calculation at 21.7s. After this moment, the proposed SM-EAC method, similar to the detailed model, continues to increase I_{rd} as the dynamic of APC. Throughout this process, I_r does not exceed the maximum value of 1.5 pu. After 30 seconds, as SEP disappears, the system accelerates and becomes unstable. Therefore, the proposed method successfully calculates the transient situation after the disturbance occurs until the SEP disappears, which is critical for transient energy calculations and stability assessment.

From Fig. 9(b), it can be seen that as the power angle and rotor current increase, the stator voltage keeps deteriorating. Since the DFIG maintains unit power factor operation during this process, Q_s varies less and I_s is closely related to I_{rd}. For the mechanical part, the rotor speed tends to stabilize at 30s due to the pitch control. However, at this moment, the SEP is already vanished, leading the DFIG to accelerate further and lose synchronization.

C. Simulation and Analysis of Multi-Swing Stability

Previous studies have effectively investigated the effects of parameters such as X_l, U_g, k_{pp}, k_{pi} and k_{ap} on system stability. In this work, we mainly focus on the relationship between k_{ai} and transient stability.

The analysis is performed using the scenario similar to case 2 in Fig. 8. While keeping other parameters and disturbance conditions constant, k_{ai} is varied across five values ranging from 0.3 to 5. Under these values, the phase plane trajectories of exponential SM-EAC are presented in Fig. 10, and the simulation results of the detailed model are depicted in Fig. 11.

All the cases eventually become unstable, which is consistent with the SM-EAC judgment. For a clearer presentation of the dynamics of the system, the instability after a longer period of time is not plotted in Fig. 11. The SM-EAC method successfully identifies three unstable cases in the third swing and two unstable cases in the first swing, which agrees with the time-domain simulations. It can be observed that increasing k_{ai} leads to an earlier and more intense instability phenomenon. While a larger k_{ai} enables faster tracking of the reference power, it also subjects the system to a larger area of acceleration and an earlier disappearance of SEP.

In the two first-swing unstable cases in Fig. 11, the system's velocity does not decelerate to 0 at the UEP and continues to accelerate on the right side of the UEP. Before the UEP, lower deceleration energy compared to higher acceleration energy led to the occurrence of instability in the first swing. In contrast, the three third-swing unstable cases depicted in Fig. 11 show the system's velocity approaching near 0 while δ increasing slowly in the third swing. In this process, the slow increase of I_{rd} in the third swing causes the SEP to rise slowly while δ continuously following the SEP. Eventually, since P_{em} and P_{ee} have no intersection, the SEP disappears, leading to the system's instability and acceleration.

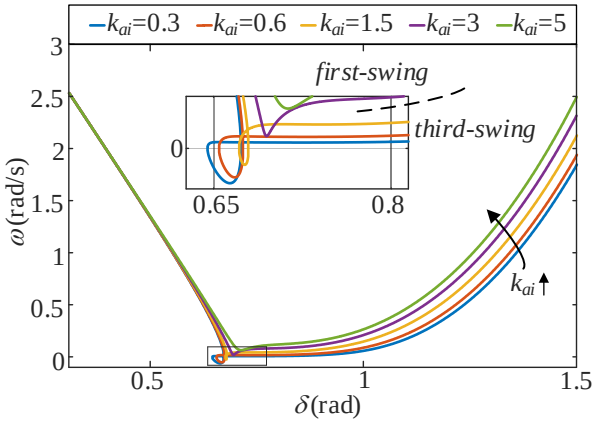

Fig. 10. Phase plane trajectories under SM-EAC with different k_{ai}.

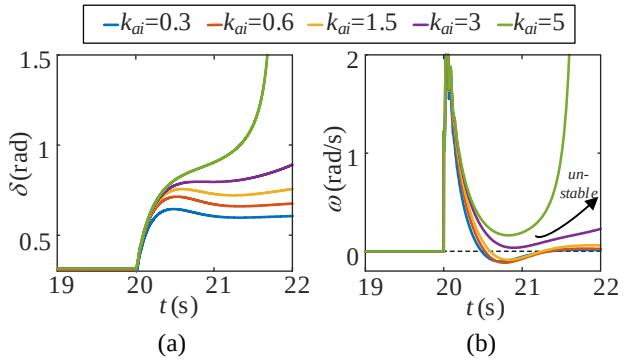

Fig. 11. Simulation results of the detailed model with different k_{ai}. (a) δ; (b) ω.

V. Conclusion

In this paper, transient modeling and stability analysis of DFIGs are investigated, which includes the dynamics of PLL and APC. To enhance the reliability of the EAC method, the proposed MD-EAC method is established to compute the damping energy analytically in each step and is further extended to be applied to multi-DFIG parallel systems. By introducing sequence mapping, the dynamic of the APC is carefully estimated. Based on these works, the SM-EAC method is presented as a recursive transient analysis method for third-order nonlinear systems. Finally, numerical simulations demonstrate the effectiveness of MD-EAC and SM-EAC. Multi-swing stability is found in numerical simulation, and the mechanism is cross-analyzed with the SM-EAC method. The main contributions of this paper are as follows:

1) The discretization allows the damping effect to be estimated accurately in MD-EAC, and the conservatism or aggressiveness in the CEAC method is resolved in various conditions.

2) The proposed exponential fitting method effectively estimates the dynamics of the APC in transient power angle variation. For APC and PLL, the different response bandwidths allow them to be analyzed by the recursive SM-EAC method.

3) The multi-swing stability is closely related to the parameter k_{ai} in the APC, and the multi-swing stability can be further strengthened by a well-selected k_{ai}.

Acknowledgment

The authors would like to thank North China Electric Power University for the support of PhD student open foundation, “Research on Stability Analysis and Advanced Control Strategy of DFIG-Based Wind Turbine”.

Appendix

TABLE I
PARAMETERS OF THE DFIG IN SIMULATION

Parameter	Value	Parameter	Value
S_n (MVA)	6*1.67	Wind speed (m/s)	11
f (Hz)	60	U_n (V, phase to phase)	575
I_{ms} ($p.u.$)	0.26	I_{max} ($p.u.$)	1.5
X_s ($p.u.$)	3.08	X_r ($p.u.$)	3.06
X_m ($p.u.$)	2.9	k_{pp}	16
k_{pi}	50		

TABLE II
PARAMETERS OF THE MULTI-DFIG PARALLEL SYSTEM

Parameter	Value	Parameter	Value
S_{base} (MVA)	6*1.67	X_{t1} ($p.u.$)	0
S_{n1} (MVA)	3*1.67	X_{t2} ($p.u.$)	0.4
S_{n2} (MVA)	3*1.67	I_{rd1} ($p.u.$)	-0.69
X_l ($p.u.$)	0.6	I_{rd2} ($p.u.$)	-0.32
Wind speed 1 (m/s)	11	Wind speed 2 (m/s)	8.5

References

[1] L. Xiong, X. Liu, Y. Liu, and F. Zhuo, ‘Modeling and Stability Issues of Voltage-source Converter-dominated Power Systems: A Review’, *CSEE J. Power Energy Syst.*, vol. 8, no. 6, pp. 1530–1549, Nov. 2022, doi: 10.17775/CSEEJPES.2020.03590.

[2] X. Wang, M. G. Taul, H. Wu, Y. Liao, F. Blaabjerg, and L. Harnefors, ‘Grid-Synchronization Stability of Converter-Based Resources—An Overview’, *IEEE Open J. Ind. Appl.*, vol. 1, pp. 115–134, 2020, doi: 10.1109/OJIA.2020.3020392.

[3] X. He and H. Geng, ‘Transient Stability of Power Systems Integrated With Inverter-Based Generation’, *IEEE Trans. Power Syst.*, vol. 36, no. 1, pp. 553–556, Jan. 2021, doi: 10.1109/TPWRS.2020.3033468.

[4] J. Hu, B. Wang, W. Wang, H. Tang, Y. Chi, and Q. Hu, ‘Small Signal Dynamics of DFIG-Based Wind Turbines During Riding Through Symmetrical Faults in Weak AC Grid’, *IEEE Trans. Energy Convers.*, vol. 32, no. 2, pp. 720–730, Jun. 2017, doi: 10.1109/TEC.2017.2655540.

[5] R. Liu, J. Yao, X. Wang, P. Sun, J. Pei, and J. Hu, ‘Dynamic Stability Analysis and Improved LVRT Schemes of DFIG-Based Wind Turbines During a Symmetrical Fault in a Weak Grid’, *IEEE Trans. Power Electron.*, vol. 35, no. 1, pp. 303–318, Jan. 2020, doi: 10.1109/TPEL.2019.2911346.

[6] X. Wang, J. Yao, J. Pei, P. Sun, H. Zhang, and R. Liu, ‘Analysis and Damping Control of Small-Signal Oscillations for VSC Connected to

Weak AC Grid During LVRT', *IEEE Trans. Energy Convers.*, vol. 34, no. 3, pp. 1667–1676, Sep. 2019, doi: 10.1109/TEC.2019.2915680.
[7] I. P. Nikolakakos, H. H. Zeineldin, M. S. El-Moursi, and J. L. Kirtley, 'Reduced-Order Model for Inter-Inverter Oscillations in Islanded Droop-Controlled Microgrids', *IEEE Trans. Smart Grid*, vol. 9, no. 5, pp. 4953–4963, Sep. 2018, doi: 10.1109/TSG.2017.2676014.
[8] M. Amin and M. Molinas, 'Small-Signal Stability Assessment of Power Electronics Based Power Systems: A Discussion of Impedance- and Eigenvalue-Based Methods', *IEEE Trans. Ind. Appl.*, vol. 53, no. 5, pp. 5014–5030, Sep. 2017, doi: 10.1109/TIA.2017.2712692.
[9] B. Hu, H. Nian, H. Li, L. Chen, S. Sahoo, and F. Blaabjerg, 'Impedance Reshaping Band Coupling and Broadband Passivity Enhancement for DFIG System', *IEEE Trans. Power Electron.*, vol. 38, no. 8, pp. 9436–9447, Aug. 2023, doi: 10.1109/TPEL.2023.3270364.
[10] M. Cespedes and J. Sun, 'Impedance Modeling and Analysis of Grid-Connected Voltage-Source Converters', *IEEE Trans. Power Electron.*, vol. 29, no. 3, pp. 1254–1261, Mar. 2014, doi: 10.1109/TPEL.2013.2262473.
[11] Y. Yang, D. Zhu, D. Zhou, X. Zou, J. Hu, and Y. Kang, 'Synchronization Instability Mechanism and Damping Enhancement Control for DFIG-Based Wind Turbine During Grid Faults', *IEEE Trans. Power Electron.*, vol. 38, no. 10, pp. 12104–12115, Oct. 2023, doi: 10.1109/TPEL.2023.3289875.
[12] 'Technical Report on the events of 9 August 2019', National Grid ESO, Sep. 2019. [Online]. Available: https://www.nationalgrideso.com/document/152346
[13] A. H. Kasem Alaboudy, H. H. Zeineldin, and J. Kirtley, 'Microgrid Stability Characterization Subsequent to Fault-Triggered Islanding Incidents', *IEEE Trans. Power Deliv.*, vol. 27, no. 2, pp. 658–669, Apr. 2012, doi: 10.1109/TPWRD.2012.2183150.
[14] W. Tang, J. Hu, Y. Chang, and F. Liu, 'Modeling of DFIG-Based Wind Turbine for Power System Transient Response Analysis in Rotor Speed Control Timescale', *IEEE Trans. Power Syst.*, vol. 33, no. 6, pp. 6795–6805, Nov. 2018, doi: 10.1109/TPWRS.2018.2827402.
[15] W. Tang, J. Hu, R. Zhang, X. Chen, and Z. Yang, 'Coupling Characteristics of DFIG-based WT Considering Reactive Power Control and Its Impact on Phase/Amplitude Transient Stability in a Rotor Speed Control Timescale', *CSEE J. Power Energy Syst.*, vol. 8, no. 2, pp. 511–522, Mar. 2022, doi: 10.17775/CSEEJPES.2020.04280.
[16] X. Fu *et al.*, 'Large-Signal Stability of Grid-Forming and Grid-Following Controls in Voltage Source Converter: A Comparative Study', *IEEE Trans. Power Electron.*, vol. 36, no. 7, pp. 7832–7840, Jul. 2021, doi: 10.1109/TPEL.2020.3047480.
[17] Y. Zhang, C. Zhang, and X. Cai, 'Large-Signal Grid-Synchronization Stability Analysis of PLL-Based VSCs Using Lyapunov's Direct Method', *IEEE Trans. Power Syst.*, vol. 37, no. 1, pp. 788–791, Jan. 2022, doi: 10.1109/TPWRS.2021.3089025.
[18] P. S. Kundur, *Power System Stability and Control*, First Edition. New York: McGraw Hill, 1994.
[19] Q. Hu, L. Fu, F. Ma, and F. Ji, 'Large Signal Synchronizing Instability of PLL-Based VSC Connected to Weak AC Grid', *IEEE Trans. Power Syst.*, vol. 34, no. 4, pp. 3220–3229, Jul. 2019, doi: 10.1109/TPWRS.2019.2892224.
[20] Y. Tang, Z. Tian, X. Zha, X. Li, M. Huang, and J. Sun, 'An Improved Equal Area Criterion for Transient Stability Analysis of Converter-Based Microgrid Considering Nonlinear Damping Effect', *IEEE Trans. Power Electron.*, vol. 37, no. 9, pp. 11272–11284, Sep. 2022, doi: 10.1109/TPEL.2022.3164687.
[21] X. Li, Z. Tian, X. Zha, P. Sun, Y. Hu, and M. Huang, 'An Iterative Equal Area Criterion for Transient Stability Analysis of Grid-tied Converter Systems with Varying Damping', *IEEE Trans. Power Syst.*, pp. 1–13, 2023, doi: 10.1109/TPWRS.2023.3241079.
[22] X. Guo *et al.*, 'Analysis and Enhancement of Active Power Transfer Capability for DFIG-Based WTs in Very Weak Grid', *IEEE J. Emerg. Sel. Top. Power Electron.*, vol. 10, no. 4, pp. 3895–3906, Aug. 2022, doi: 10.1109/JESTPE.2021.3089235.
[23] Q. Hu, L. Fu, F. Ma, G. Wang, C. Liu, and Y. Ma, 'Impact of LVRT Control on Transient Synchronizing Stability of PLL-Based Wind Turbine Converter Connected to High Impedance AC Grid', *IEEE Trans. Power Syst.*, pp. 1–13, 2022, doi: 10.1109/TPWRS.2022.3223675.
[24] F. Zhao, Z. Shuai, W. Huang, Y. Shen, Z. J. Shen, and C. Shen, 'A Unified Model of Voltage-Controlled Inverter for Transient Angle Stability Analysis', *IEEE Trans. Power Deliv.*, vol. 37, no. 3, pp. 2275–2288, Jun. 2022, doi: 10.1109/TPWRD.2021.3109007.
[25] S. Chen *et al.*, 'Transient Stability Analysis and Improved Control Strategy for DC-Link Voltage of DFIG-Based WT During LVRT', *IEEE Trans. Energy Convers.*, vol. 37, no. 2, pp. 880–891, Jun. 2022, doi: 10.1109/TEC.2021.3126855.
[26] C. Shen, W. Gu, W. Sheng, and K. Liu, 'Transient stability analysis and design of VSGs with different DC-link voltage controllers', *CSEE J. Power Energy Syst.*, pp. 1–11, 2023, doi: 10.17775/CSEEJPES.2022.03300.
[27] M. Yin, C. Y. Chung, K. P. Wong, Y. Xue, and Y. Zou, 'An Improved Iterative Method for Assessment of Multi-Swing Transient Stability Limit', *IEEE Trans. Power Syst.*, vol. 26, no. 4, pp. 2023–2030, Nov. 2011, doi: 10.1109/TPWRS.2011.2109970.
[28] X. Liu *et al.*, 'Fault Current Unified Calculation Method for Whole Process Fault Ride-Through of DFIG-Based Wind Farms', *IEEE Trans. Smart Grid*, pp. 1–1, 2023, doi: 10.1109/TSG.2023.3270702.
[29] Y. Ma, D. Zhu, Z. Zhang, X. Zou, J. Hu, and Y. Kang, 'Modeling and Transient Stability Analysis for Type-3 Wind Turbines Using Singular Perturbation and Lyapunov Methods', *IEEE Trans. Ind. Electron.*, vol. 70, no. 8, pp. 8075–8086, Aug. 2023, doi: 10.1109/TIE.2022.3210484.
[30] H. Yuan, X. Yuan, and J. Hu, 'Modeling of Grid-Connected VSCs for Power System Small-Signal Stability Analysis in DC-Link Voltage Control Timescale', *IEEE Trans. Power Syst.*, vol. 32, no. 5, pp. 3981–3991, Sep. 2017, doi: 10.1109/TPWRS.2017.2653939.
[31] J. Hu, H. Yuan, and X. Yuan, 'Modeling of DFIG-Based WTs for Small-Signal Stability Analysis in DVC Timescale in Power Electronized Power Systems', *IEEE Trans. Energy Convers.*, vol. 32, no. 3, pp. 1151–1165, Sep. 2017, doi: 10.1109/TEC.2017.2701886.
[32] Y. Xue, T. Van Custem, and M. Ribbens-Pavella, 'Extended equal area criterion justifications, generalizations, applications', *IEEE Trans. Power Syst.*, vol. 4, no. 1, pp. 44–52, Feb. 1989, doi: 10.1109/59.32456.
[33] N. W. Miller, J. J. Sanchez-Gasca, W. W. Price, and R. W. Delmerico, 'Dynamic modeling of GE 1.5 and 3.6 MW wind turbine-generators for stability simulations', in *2003 IEEE Power Engineering Society General Meeting (IEEE Cat. No.03CH37491)*, Jul. 2003, pp. 1977-1983 Vol. 3. doi: 10.1109/PES.2003.1267470.

Ruibo Li (Student Member, IEEE) was born in Handan, China, in 1997. He received the B.E. degree in electrical engineering from North China Electric Power University, Baoding, China, in 2019. He is pursuing the Ph.D. degree now in North China Electric Power University, Beijing, China. He is currently a visiting Ph.D. student with the AAU Energy, Aalborg University, Aalborg, Denmark. He also works in the Key Laboratory of Distributed Energy Storage and Microgrid in Hebei Province. His research interests include modeling, control and stability analysis of grid-connected DFIG.

Xiangwu Yan (Member, IEEE) received the B.E. degree in electrical engineering from Hunan University, Hunan, China, in 1986, the M.S. degree from North China Electric Power University, Baoding, China, in 1990, and the Ph.D. degree from the Harbin Institute of Technology, Heilongjiang, China, in 1997. He was an Honorary Fellow of the Wisconsin Electric Machines and Power Electronics Consortium (WEMPEC) with the University of Wisconsin-Madison, Madison. Then, he returned to the North China Electric Power University as a Faculty Member, where he continues to direct research in various areas of electronic

power conversion. He has published more than 100 technical publications, including more than 30 China patents, and has won five provincial and ministerial science and technology awards.

Qi Zhang (Student Member, IEEE) received the B.Eng and M.Sc in electrical engineering from China University of Mining and Technology (Beijing), Beijing, China, in 2015 and 2018, respectively, and the Ph.D. degree in energy technology from Aalborg university, Aalborg, Denmark, in 2023. Currently, he works as a postdoc at AAU ENERGY, Aalborg University, Aalborg, Denmark.
His main research interests include modeling, control, fault analysis and transient stability of power electronic dominated power system; control of power electronic converters, selective harmonic elimination, HVDC transmission system, HVDC tapping technology.

Yanbo Wang (Senior Member, IEEE) received Ph.D. degree in Electrical Engineering at the Department of Energy Technology, Aalborg University, Denmark, in 2017. He is an Associate Professor with the Department of Energy Technology, Aalborg University, Denmark. He is the vice leader of Wind Power System Research program at the Department of Energy Technology, Aalborg University. From June to October of 2016, he was a visiting scholar in Power System Research Group of the Department of Electrical and Computer Engineering, University of Manitoba, Winnipeg, MB, Canada. His research interests include distributed power generation system, wind power system, microgrid, and power electronic-dominated power system, etc.

Zhe Chen (Fellow, IEEE) received the B.Eng. and M.Sc. degrees from Northeast China Institute of Electric Power Engineering, Jilin City, China, and the Ph.D. degree from University of Durham, U.K.
Dr. Chen is a full Professor with the Department of Energy Technology, Aalborg University, Denmark. He is the leader of Wind Power System Research program at the Department of Energy Technology, Aalborg University and the Danish Principle Investigator for Wind Energy of Sino-Danish Centre for Education and Research. His research areas are power systems, power electronics and electric machines, and his main current research interests are wind energy and modern power systems. Dr. Chen is an Associate Editor of the IEEE Transactions on Power Electronics, a member of editorial boards for many international journals, a Fellow of the Institution of Engineering and Technology (IET, London, U.K.), and a Chartered Engineer in the U.K.